PERGAMON

International Journal of Solids and Structures 37 (2000) 2341–2358

INTERNATIONAL JOURNAL OF SOLIDS and STRUCTURES

www.elsevier.com/locate/ijsolstr

On the dynamic behaviour of porous materials

R. Paskaramoorthy[a,*], S.A. Meguid[b]

[a]*School of Mechanical Engineering, University of the Witwatersrand, Private Bag 3, Wits, 2050, South Africa*
[b]*The Engineering Mechanics and Design Laboratory, Department of Mechanical Engineering, University of Toronto, 5 King's College Road, Toronto, Ontario, M5S 1A4, Canada*

Received 5 September 1998; in revised form 6 November 1998

Abstract

The mechanical properties of porous materials are strongly influenced by the stress concentration around pores. In view of this, stress fields around a spheroidal pore is studied under dynamic loading conditions. A hybrid method that combines the finite element method with an analytical approach has been used. It is shown that the dynamic stress concentration is influenced by three parameters: frequency of excitation, geometry of the pore and Poisson's ratio of the medium. It is also shown that the dynamic stress concentration can reach much higher values than that predicted by static analysis. © 2000 Published by Elsevier Science Ltd. All rights reserved.

1. Introduction

Stress concentrations in elastic bodies arise from the presence of geometric and material discontinuities, such as cavities, cracks, notches, inclusions and reinforcements. Determination of stress concentration is a problem of considerable interest in many branches of applied mechanics, since failure of a structural member often initiates as a result of high concentration of stress.

The study of stress concentration goes back to Kirsch (1898) who considered a circular hole in an infinite plate subjected to static tensile loading. Many investigations have since been conducted with various kinds of discontinuities. A comprehensive survey of the literature may be found, for instance, in the review articles of Sternberg (1958) and Neuber and Hahn (1966). Most of these investigations considered static loading, where the inertia of the medium can be ignored. Under dynamic loading, however, the inertia of the medium plays a significant role. The action of the applied dynamic load is transmitted in the form of waves traveling through the medium. At a discontinuity, these waves are reflected, refracted and scattered giving rise to a complex stress pattern and, often to high elevation of

* Corresponding author. Fax: +27-11-339-7997.
E-mail address: moorthy@hertz.mech.wits.ac.za (R. Paskaramoorthy)

0020-7683/00/$ - see front matter © 2000 Published by Elsevier Science Ltd. All rights reserved.
PII: S0020-7683(98)00319-9

local stresses. The phenomenon of dynamic stress concentration may, therefore, be regarded as one of scattering of elastic waves.

Scattering of elastic waves by a discontinuity has been the subject of many investigations. The excellent monograph by Pao and Mow (1973) gives a comprehensive coverage of this and other related subjects. Recent results have been presented by Bogan and Hinders (1993) for a two-dimensional geometry. In three dimensions, the spherical discontinuity problems are perhaps the easiest to solve. Scattering by a spheriodal discontinuity presents considerably greater analytical and computational difficulties than does the three-dimensional spherical geometry problems. Datta (1997) and Willis (1980) presented approximate asymptotic solutions valid at low frequencies. In recent years, Paskaramoorthy et al. (1988), Olsson et al. (1990), and Meguid and Wang (1997) have presented results obtained by using numerical techniques. In all these studies, the emphasis was on the scattered wave pattern, and none analyzed, in detail, the stress concentration near the spheroidal discontinuity.

In the material science literature relating to this topic, the influence of stress concentration around pores on the mechanical properties of porous materials has long been recognized (Hasselman and Fulrath, 1964; Rossi, 1968; Wang, 1984; Panakkal et al., 1990; Maitra and Phani, 1994; Boccaccini et al., 1995). For instance, an equation of the form

$$E = E_0(1-p)^m$$

has been shown to predict the Young's modulus (E) of sintered powder metals and porous ceramics (Panakkal et al., 1990; Maitra and Phani, 1994). In the above, E_0 is the Young's modulus of the non-porous material, p is the volume fraction of pores and m is related to the stress concentration factor around the pores. Similar relationships have also been proposed to calculate the fracture strength of porous materials (Danninger et al., 1993).

In this paper, we study the stress concentration around pores under dynamic loading. The pores are idealised to have spheroidal geometries. For simplicity, the effect of the interaction of neighbouring pores is ignored. Therefore, the results are valid for low volume fraction of pores. The geometry of a single pore embedded in an infinitely large matrix is depicted in Fig. 1a where the z-axis is the symmetry axis, $2a$ and $2b$ being the diameters of the pore along the x- and z-axes, respectively. The spheroidal pore is said to be prolate for $b/a > 1$ and oblate for $b/a < 1$. The simplest form of dynamic excitation is a plane harmonic dilatational wave propagating along this axis of symmetry. The resulting stress field is axisymmetric. While the corresponding static problem may be solved in closed form, the dynamic problem does not lend itself to a simple solution. The difficulty is associated with the complex scattering phenomenon. The solution of the problem will be described using both cylindrical and spherical coordinate systems shown in Fig. 1. To solve the problem, we use a hybrid method that combines the finite element technique with analytical functions. In this approach, a fictitious spherical boundary B enclosing the pore is drawn. The region inside this boundary, referred to as the interior region, is modelled through an assemblage of conventional finite elements. The region outside B, referred to as the exterior region, is represented by spherical wave functions. Coupling of the interior and exterior region solutions is achieved by imposing the continuity of displacements and tractions along the common boundary B. This leads to a set of linear equations that enables the displacements and stresses at any point to be determined. The concept of the hybrid method is quite general and it has been successfully applied to solve several two- and three-dimensional elastodynamic problems (Dong, 1981; Goetschel et al., 1982; Datta and Shah, 1982; Avanessian et al., 1986, 1989; Paskaramoorthy et al., 1988, 1989).

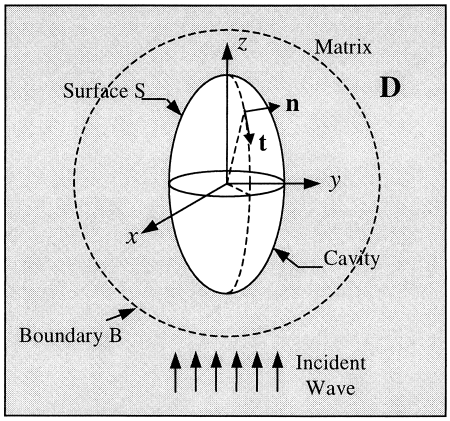

a. Schematic of the problem

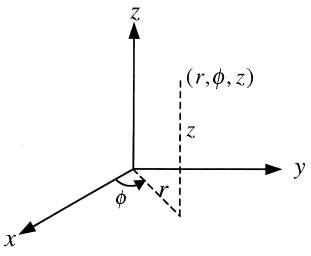

b. Cylindrical coordinate system

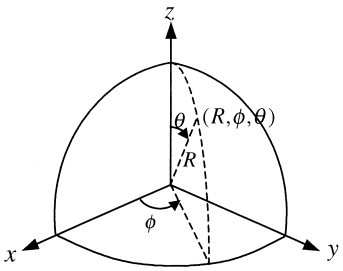

c. Spherical coordinate system

Fig. 1. Problem geometry with cylindrical and spherical coordinate systems.

2. Statement of the problem

The surface of the pore, denoted by S, may be defined by

$$\frac{x^2}{a^2}+\frac{y^2}{a^2}+\frac{z^2}{b^2}=1. \tag{1}$$

The domain of the medium is denoted by D. The material is assumed to be homogeneous, linearly elastic and isotropic. Only time-harmonic excitation is considered. Thus, all the field quantities have a time dependence $e^{-i\omega t}$, where ω is the frequency of excitation. The time dependence is suppressed in all the subsequent representations for notational convenience.

The equation of motion of the domain D for the steady state is specified by

$$(\lambda+2\mu)\nabla(\nabla\cdot\mathbf{U})-\mu\nabla\times\nabla\times\mathbf{U}+\rho\omega^2\mathbf{U}=0 \quad \mathbf{x}\in D \tag{2}$$

where $\mathbf{U} = (u, v, w)$ is the displacement vector, $\mathbf{x}$ is the position vector, ρ is the density, and λ and μ are Lamé constants of the medium.

The boundary condition on the surface S are of the form

$$\sigma_{ij} n_j = 0 \quad \mathbf{x} \in S \tag{3}$$

where $\mathbf{n}$ is the unit normal vector to the surface S and the summation convention for repeated indices is assumed. A solution of eqn (2) satisfying eqn (3) is sought. It should be noted that the solution should also be regular at infinity.

3. Formulation of the problem

3.1. Interior region

This region is modelled by using finite elements. The motion of this region may be perceived as a forced vibration with the incident and scattered waves providing the forcing functions at the boundary B. The governing equations of motion can be obtained by following the conventional discretization process of the finite element methodology for axisymmetric elements, and are written as

$$[S]\{q\} = \{P\} \tag{4}$$

where

$$[S] = [K] - \omega^2[M] \tag{5}$$

in which $[K]$ and $[M]$ are the respective stiffness and consistent mass matrices of the interior region, $\{q\}$ is the vector of nodal displacements, and $\{P\}$ is the vector of nodal loads that has non-zero components corresponding to the interface degrees of freedom only. It should be noted that eqn (4) is formulated in a cylindrical coordinate system as shown in Fig. 1b. Thus, the array $\{q\}$ contains radial and axial displacements at the nodes.

If the vector $\{q\}$ is separated into two parts, $\{q_B\}$ corresponding to nodal displacement at the boundary B, and $\{q_I\}$ corresponding to nodal displacements elsewhere in the interior region, eqn (4) can be written as

$$\begin{bmatrix} S_{II} & S_{IB} \\ S_{BI} & S_{BB} \end{bmatrix} \begin{Bmatrix} q_I \\ q_B \end{Bmatrix} = \begin{Bmatrix} 0 \\ P_B \end{Bmatrix} \tag{6}$$

in which the $\{P_B\}$ represent the interaction forces between the interior and exterior regions.

3.2. Exterior region

The displacement vector $\mathbf{U}$ in this region consists of the incident and scattered fields which are denoted by the superscripts i and s, respectively. A solution for $\mathbf{U}^s$ satisfying eqn (2) and far-field radiation conditions can be written in the spherical coordinate system of Fig. 1c as

$$\mathbf{U}^s = \nabla\phi + \nabla \times \nabla \times (\mathbf{e}_R R\chi) \tag{7}$$

where

$$\phi = \Sigma a_{1n} h_n(\alpha R) P_n(\cos\theta) \tag{8}$$

$$\chi = \Sigma a_{2n} h_n(\beta R) P_n(\cos\theta). \tag{9}$$

In the above, and in the following, all the summations are over integral values of n from zero to infinity, $\mathbf{e}_R$ is the unit vector along the R-direction, a_{1n} and a_{2n} are as yet unknown amplitude coefficients, h_n is the spherical Hankel function of the first kind, P_n is the Legendre polynomial, α and β are wave numbers defined by

$$\alpha^2 = \frac{\omega^2\rho}{(\lambda+2\mu)}; \qquad \beta^2 = \frac{\omega^2\rho}{\mu}. \tag{10}$$

Substitution of eqns (8) and (9) in eqn (7) leads to

$$u_R^s = \Sigma\left[a_{1n} g_{1n}^R + a_{2n} g_{2n}^R\right] P_n \tag{11}$$

$$u_\theta^s = \Sigma\left[a_{1n} g_{1n}^\theta + a_{2n} g_{2n}^\theta\right] \frac{\mathrm{d}P_n}{\mathrm{d}\theta} \tag{12}$$

where

$$g_{1n}^R = \frac{n}{R} h_n(\alpha R) - \alpha h_{n+1}(\alpha R) \tag{13}$$

$$g_{2n}^R = n(n+1)\frac{h_n(\beta R)}{\beta R} \tag{14}$$

$$g_{1n}^\theta = \frac{h_n(\alpha R)}{R} \tag{15}$$

$$g_{2n}^\theta = (n+1)\frac{h_n(\beta R)}{\beta R} - h_{n+1}(\beta R). \tag{16}$$

The stress field associated with the scattered waves can be derived from the displacements in eqns (11) and (12).

$$\sigma_{RR}^s = \Sigma\left[a_{1n} f_{1n}^R + a_{2n} f_{2n}^R\right] P_n \tag{17}$$

$$\sigma_{R\theta}^s = \Sigma\left[a_{1n} f_{1n}^\theta + a_{2n} f_{2n}^\theta\right] \frac{\mathrm{d}P_n}{\mathrm{d}\theta} \tag{18}$$

where

$$f_{1n}^R = \frac{2\mu}{R^2}\left[\left(n^2 - n - \frac{1}{2}\alpha^2 R^2\right) h_n(\alpha R) + 2\alpha R h_{n+1}(\alpha R)\right] \tag{19}$$

$$f_{2n}^R = \frac{2\mu}{R^2}\frac{n(n+1)}{\beta}\left[(n-1)h_n(\beta R) - \beta R h_{n+1}(\beta R)\right] \tag{20}$$

$$f^{\theta}_{1n} = \frac{2\mu}{R^2}\left[(n-1)h_n(\alpha R) - \alpha R h_{n+1}(\alpha R)\right] \tag{21}$$

$$f^{\theta}_{2n} = \frac{2\mu}{R^2}\left[\left(n^2 - 1 - \frac{1}{2}\beta^2 R^2\right)h_n(\beta R) + \beta R h_{n+1}(\beta R)\right]. \tag{22}$$

Now let p be the number of significant wave functions in eqns (8), (9), (11), (12), (17) and (18). Evaluating eqns (11) and (12) at each of the nodes lying on the boundary B, we can construct a matrix $[G]$ relating the nodal displacements to the unknown coefficients as

$$\{q^s_B\}_{\text{sph}} = [G]\{a\} \tag{23}$$

where $\{q^s_B\}_{\text{sph}}$ is the array of displacements, in spherical coordinates, due to the scattered field at the nodes on the boundary B, $\{a\}$ contains the unknown coefficients a_{1n} and a_{2n} with $n = 0, 1, \ldots, p-1$. It should be noted that the matrix $[G]$ is complex valued, and has dimension $2N_B \times 2p$ with N_B being the number of nodes on the boundary B.

Similarly, a relationship between the nodal forces at the boundary B, $\{P^s_B\}$, and the unknown coefficients $\{a\}$ can be established by evaluating the stresses σ^s_{RR} and $\sigma^s_{R\theta}$ at each of the nodes on B and multiplying them by the corresponding tributary area:

$$\{P^s_B\}_{\text{sph}} = [F]\{a\}. \tag{24}$$

We can now establish a relationship between the load vector $\{P^s_B\}$ and the displacement vector $\{q^s_B\}$ by eliminating $\{a\}$ from eqns (23) and (24). To this end, we first write eqn (23) as (see Appendix)

$$\{a\} = [H]\{q^s_B\}_{\text{sph}}; \quad [H] = \left([G^*]^{\mathrm{T}}[G]\right)^{-1}[G^*]^{\mathrm{T}} \tag{25}$$

and substitute it in eqn (24) to obtain

$$\{P^s_B\}_{\text{sph}} = [F][H]\{q^s_B\}_{\text{sph}}. \tag{26}$$

The arrays $\{P^s_B\}$ and $[q^s_B\}$ in the above equation are in the spherical coordinate system. When they are transformed into cylindrical coordinates, eqn (26) takes the form

$$\left\{P^s_B\right\} = \left[S_f\right]\left\{q^s_B\right\} \tag{27}$$

where

$$[S_f] = [T]^t[F][H][T]$$

in which $[T]$ is the transformation matrix.

3.3. Incident field

The incident field is specified by

$$\mathbf{U}^i = \nabla\phi^i; \qquad \phi^i = \mathrm{e}^{i\alpha z}. \tag{28}$$

As indicated earlier, this is a plane P-wave, and it propagates in the direction of the positive z-axis. The displacements and stresses induced by this wave field have the following explicit forms:

$$u^i_r = 0 \tag{29}$$

$$u_z^i = i\alpha\, e^{i\alpha z} \tag{30}$$

$$\sigma_{zz}^i = -\mu\beta^2 e^{i\alpha z} \tag{31}$$

$$\sigma_{rr}^i = -\lambda\alpha^2 e^{i\alpha z} \tag{32}$$

$$\sigma_{rz}^i = 0. \tag{33}$$

By evaluating these expressions at the nodes on the boundary B, the arrays $\{q_B^i\}$ and $\{P_B^i\}$ can be formed.

3.4. Global solution

The continuity of displacements and stresses across the boundary B can be imposed by setting the displacements and stresses from the interior region to be equal to those from the exterior region:

$$\{q_B\} = \{q_B^i\} + \{q_B^s\} \tag{34}$$

$$\{P_B\} = \{P_B^i\} + \{P_B^s\}. \tag{35}$$

In view of eqns (34), (35) and (27), eqn (6) may be written as

$$\begin{bmatrix} S_{II} & S_{IB} \\ S_{BI} & S_{BB} - S_f \end{bmatrix} \begin{Bmatrix} q_I \\ q_B \end{Bmatrix} = \begin{Bmatrix} 0 \\ P_B^i - S_f q_B^i \end{Bmatrix}. \tag{36}$$

Once the above equation is solved for the nodal displacements, the unknown amplitudes of the scattered field may be obtained from eqns (25).

4. Numerical results and discussion

We have used spherical functions in eqns (7)–(9) to construct a scattered-field solution in the exterior region. This representation of exterior region by spherical functions is unique and complete (Morse and Feshbach, 1953). In writing eqn (23), we have considered only a finite number of wave functions. This will not introduce any significant error since the contribution of the higher-order terms of the infinite series in eqn (23) and in other equations is small, but care should be taken to include a sufficient number of spherical functions. The actual number of spherical functions required is determined by conducting numerical experiments on the convergence of the solution. Also, the spherical wave functions should be taken in sequence. That is to say, no preference be given to a higher-order spherical function at the omission of a lower-order function. More details may be found in the excellent article by Dong that reviews the hybrid method in its generality and addresses issues related to convergence, completeness and uniqueness of the solution.

In this study, the dynamic excitation is provided by an incident P-wave defined by eqn (28). In the absence of the pore, the stress field at any point in the medium is expressed in rectangular coordinates as

$$\sigma_{xx} = -\lambda\alpha^2 e^{i\alpha z - i\omega t} \tag{37}$$

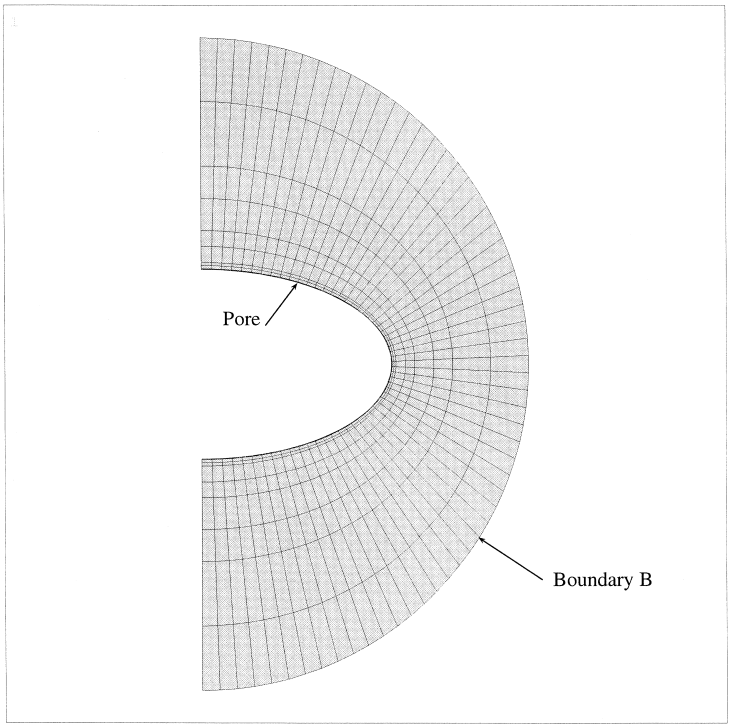

Fig. 2. Finite element mesh of the interior region for $b/a = 0.5$.

$$\sigma_{yy} = -\lambda\alpha^2 e^{i\alpha z - i\omega t} \tag{38}$$

$$\sigma_{zz} = -\mu\beta^2 e^{i\alpha z - i\omega t} \tag{39}$$

$$\sigma_{xy} = \sigma_{yz} = \sigma_{zx} = 0. \tag{40}$$

Since all the shear stresses are zero, all the normal stresses are principal stresses and the maximum value is $\sigma_0 = \mu\beta^2$.

In the presence of the pore, the stress field is significantly different from that given by eqns (37)–(40) due to scattering. In these problems, the primary interest is in the tangential stress σ_{tt} and the hoop stress $\sigma_{\phi\phi}$ where $\mathbf{t}$ is the tangential vector to the surface of the pore and ϕ is the azimuthal direction in the spherical coordinate system (Fig. 1). These stresses are expressed in dimensionless forms by normalizing with respect to the amplitude of the incident wave, σ_0:

$$\bar{\sigma}_{tt} = \left.\frac{\sigma_{tt}}{\sigma_0}\right|_{R=a}; \quad \bar{\sigma}_{\phi\phi} = \left.\frac{\sigma_{\phi\phi}}{\sigma_0}\right|_{R=a}.$$

Thus, the values of the $\bar{\sigma}_{tt}$ and $\bar{\sigma}_{\phi\phi}$ can be considered as dynamic stress concentration factors. These are computed for various frequencies from the nodal displacements of eqn (36) by following standard finite element procedures. The nature of the dynamic excitation is better appreciated by considering the

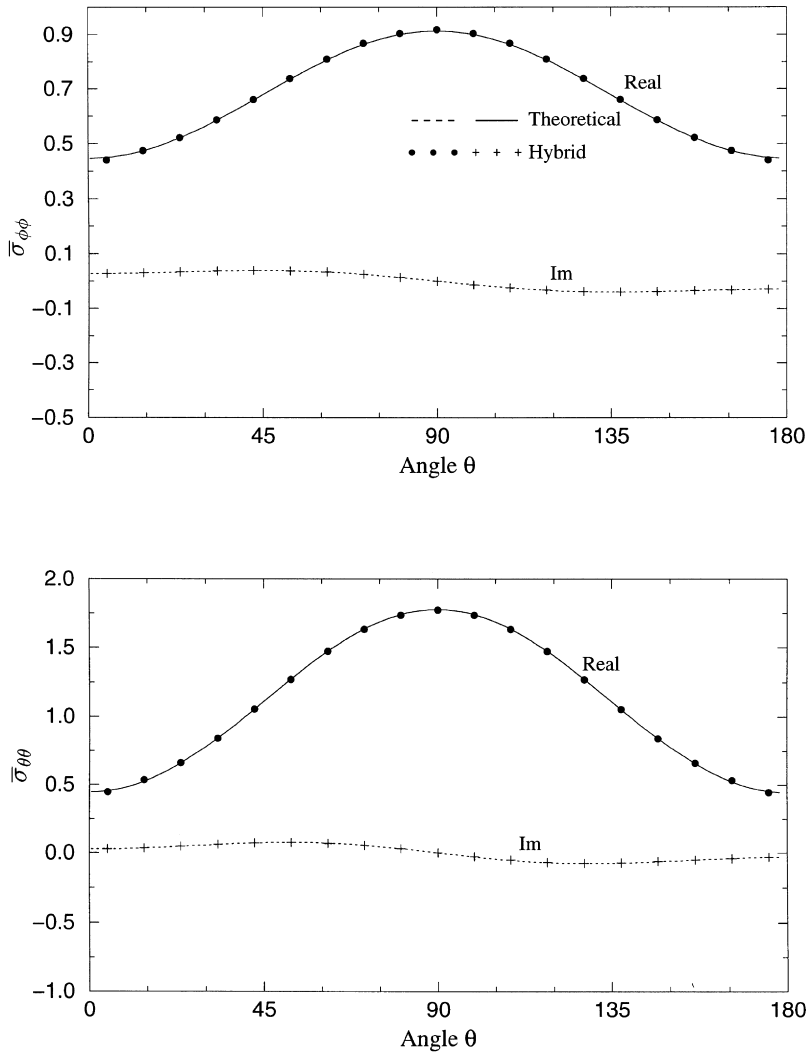

Fig. 3. Comparison of stresses along the circumference of a spherical pore for $\alpha a = 0.1$.

limiting static case. When the frequency approaches zero, the applied stress field at infinity approaches

$$\sigma_{zz} = -\sigma_0 \tag{41}$$

$$\sigma_{xx} = \sigma_{yy} = -\frac{\nu}{1-\nu}\sigma_0 \tag{42}$$

$$\sigma_{xy} = \sigma_{yz} = \sigma_{zx} = 0 \tag{43}$$

where σ_0 is a constant. The stress field of eqns (41)–(43) is triaxial. Thus, the results presented herein are

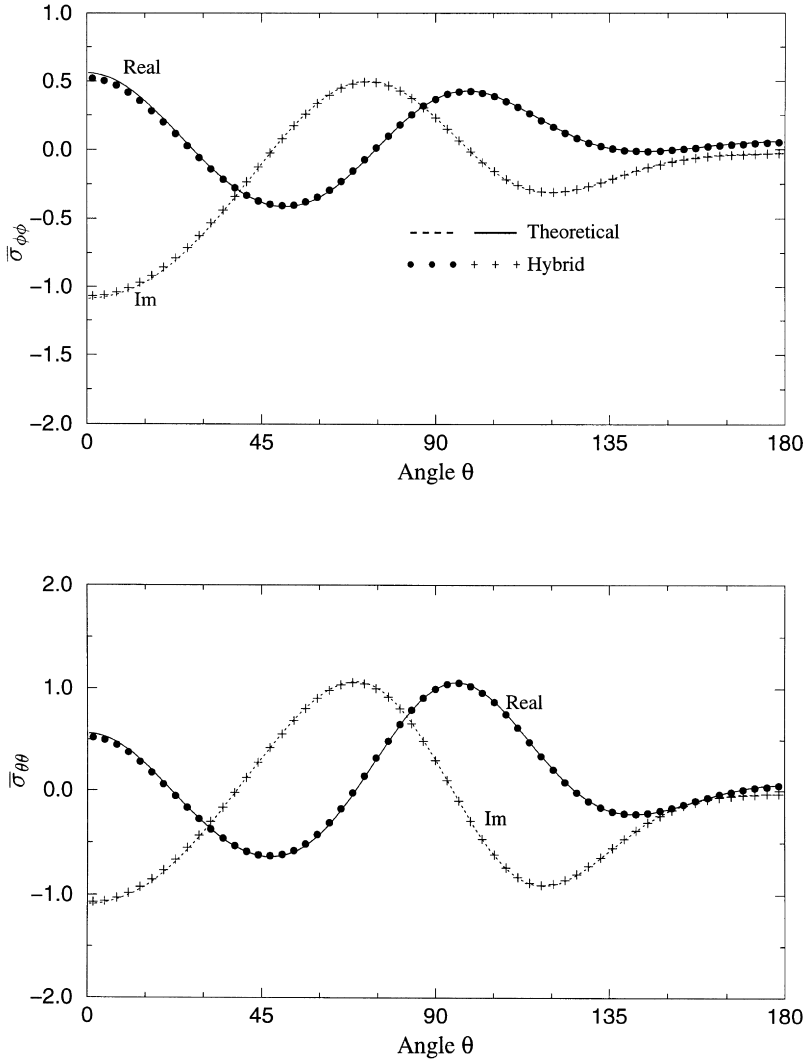

Fig. 4. Comparison of stresses along the circumference of a spherical pore for $\alpha a = 3.0$.

for the dynamic counterpart of this triaxial load. A typical finite element mesh of the interior region is shown in Fig. 2. Refinement of the mesh may be necessary for high frequency excitations. The results have the general form

$$\sigma = (R + iI)\mathrm{e}^{-i\omega t}$$

where the real part R represents the solution at $t = 0$ and $T/2$, and the imaginary part I represents the solution at $t = T/4$ and $3T/4$, T being the period of excitation. The absolute value $(R^2 + I^2)^{1/2}$ is the maximum stress which occur at some instant depending on the phase-shift.

In order to assess the accuracy of the numerical procedure, stresses on the surface of a spherical pore

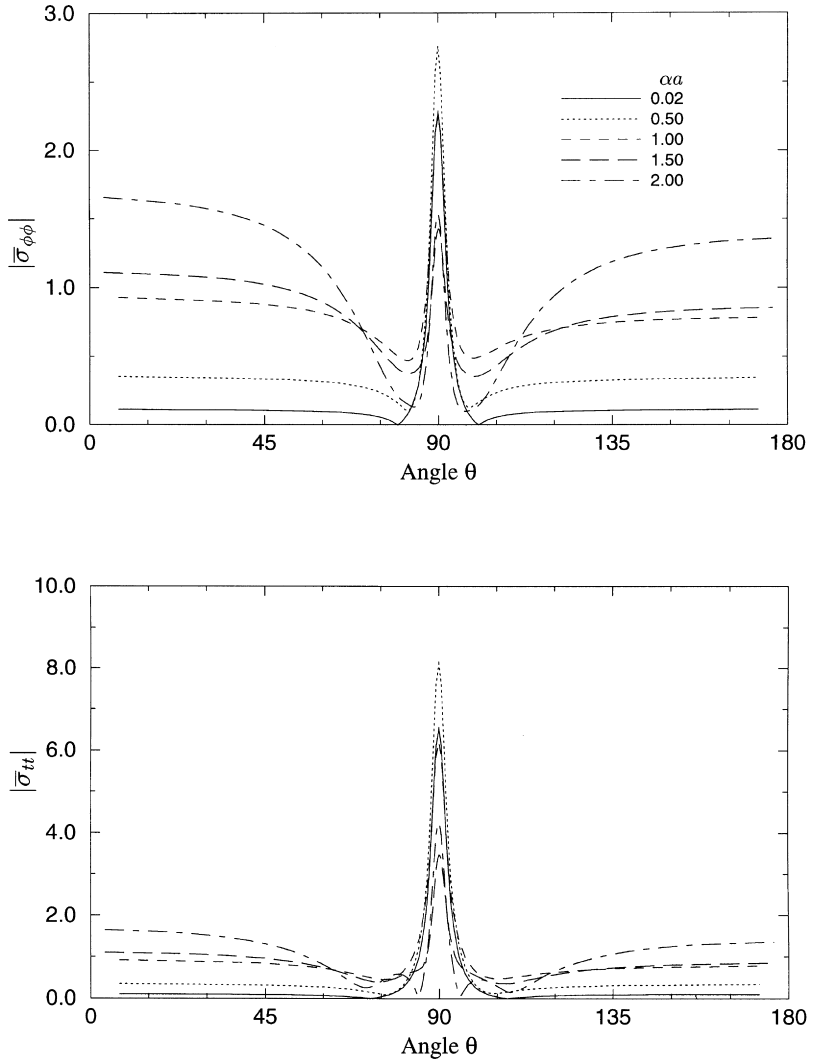

Fig. 5. Angular distribution of stresses on the surface of the cavity ($\nu = 0.35$, $b/a = 0.2$).

of radius a were computed by the present method and compared with the analytical solution. In Figs. 3 and 4, the results are presented in nondimensional form for two representative values of dimensionless wave numbers 0.1 and 3.0. Agreement between the analytical and numerical results can be seen to be excellent. The wavelength corresponding to the nondimensional wave number 0.1 is approximately 30 times the diameter of the pore. At this wavelength, there is little dynamic effects present. For the nondimensional wave number 3.0, the wavelength is about the same as the diameter of the pore and significant dynamic interaction is expected.

We may now consider a pore having a spheroidal geometry. This problem can be solved analytically by using spheroidal coordinates. The mathematics of this approach is, however, complex and intricate. We have solved the problem by using the hybrid approach described earlier. Figures 5 and 6 illustrate

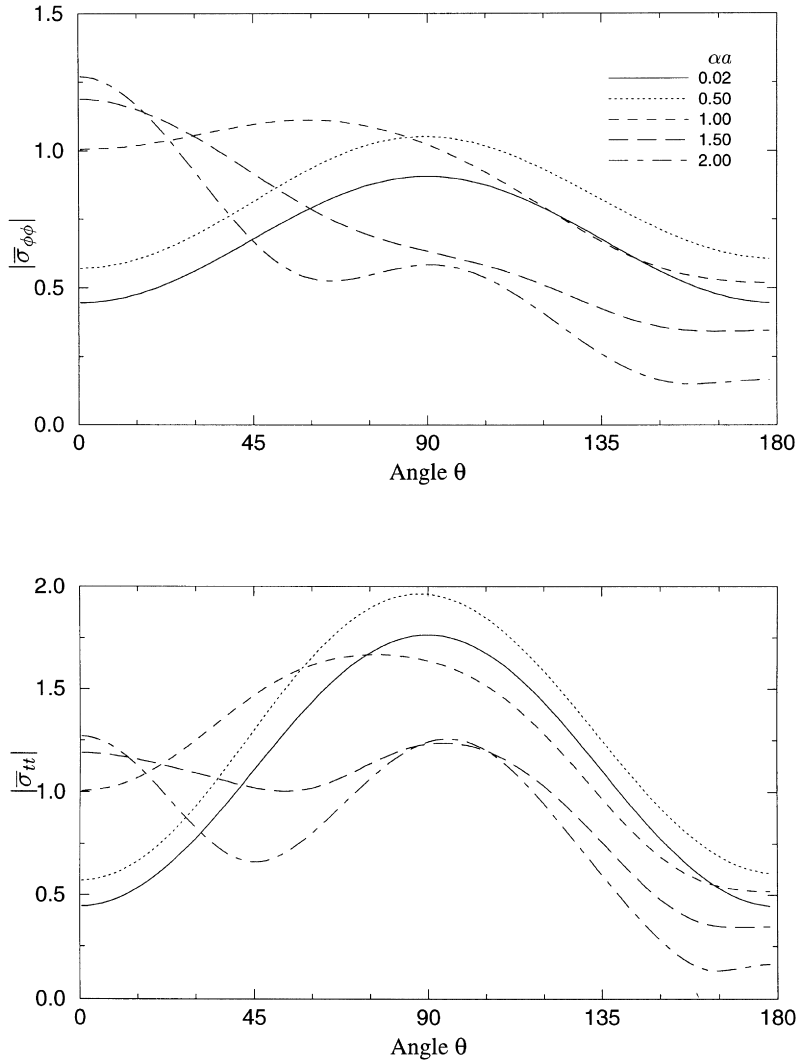

Fig. 6. Angular distribution of stresses on the surface of the cavity ($\nu = 0.35$, $b/a = 1.0$).

the angular distribution of $\bar{\sigma}_{tt}$ and $\bar{\sigma}_{\phi\phi}$ for five wave numbers αa = 0.02, 0.5, 1.0, 1.5 and 2.0. For $\alpha a = 0.02$, the frequency is very small and the wavelength is approximately 150 times the diameter of the pore. At this wave number, hardly any dynamic effect is expected, and the dynamic solution can be regarded to represent the quasi-static solution. The applied loading for this wave number is given approximately by eqns (41)–(43), and exhibits symmetry with respect to the $z = 0$ plane. The resulting stress field must also be symmetric about this plane. This is evident from these Figures. At other wave numbers, the applied stress fields is not symmetric since the incident wave only illuminates the bottom half of the pore; the top half of the pore is in the shadow region. The scattering phenomenon then dominates, considerably distorting the results from the quasi-static solution. It is apparent that the aspect ratio and hence the geometry of the pore has a strong influence on the stresses. As the aspect

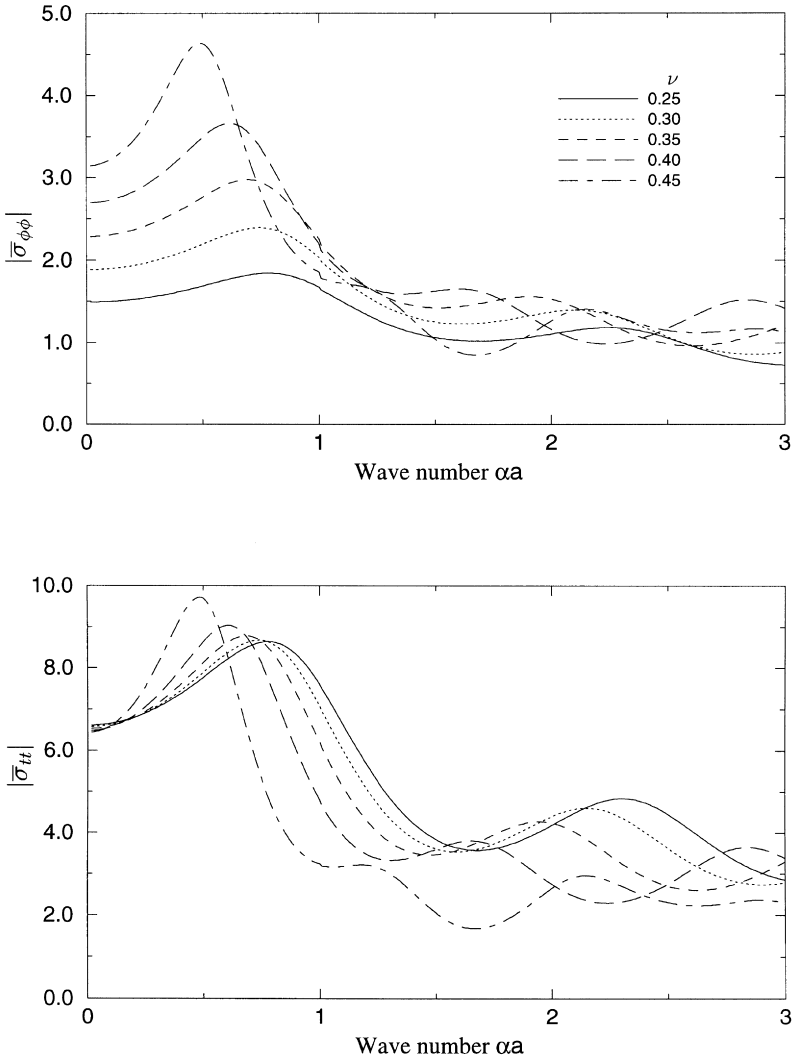

Fig. 7. Effect of frequency on stresses at $\theta = \pi/2$ for $b/a = 0.2$.

ratio increases, the maximum values of stresses decrease. The excitation frequency also seems to have a strong influence on the stresses. For $\alpha a = 0.02$, maxima for both $\bar{\sigma}_{\phi\phi}$ and $\bar{\sigma}_{tt}$ occur at $\theta = \pi/2$. As the frequency increases, the stresses at $\theta = \pi/2$ first increase and then decrease. At the same time, the stresses in the shadow region of the pore increases while the stresses in the incident side of the pore decrease. The location of the maximum stress also shifts to the shadow side of the pore. This shift seems to be more pronounced for $\bar{\sigma}_{\phi\phi}$ than for $\bar{\sigma}_{tt}$. In the case of $b/a = 1$, for example, maximum of $\bar{\sigma}_{\phi\phi}$ occurs at $\theta = 0$ for αa greater than 1.0.

In Figs. 7 and 8, $\bar{\sigma}_{tt}$ and $\bar{\sigma}_{\phi\phi}$ at $\theta = \pi/2$ are shown as a function of the incident wave number for five values of Poisson's ratio. A separate static analysis confirmed that as αa approaches zero, the dynamic stresses approach the corresponding static values. It can be seen that in the high frequency end of the

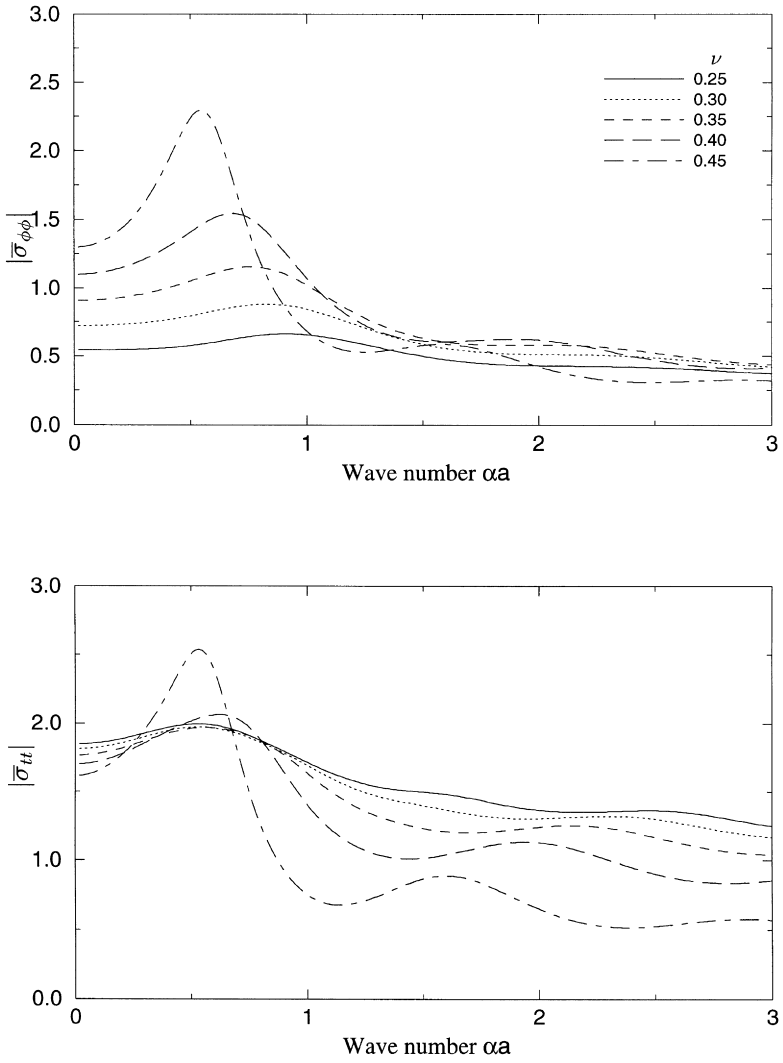

Fig. 8. Effect of frequency on stresses at $\theta = \pi/2$ for $b/a = 1.0$.

range considered, the dynamic stresses are lower than the static values. The dynamic stresses reach their maxima when the wave number αa is between 0.5 and 1.0 and that the maximum dynamic stresses are 10–50% higher than the static values. In the case of $b/a = 0.2$ and $\nu = 0.35$, for example, maximum value of $\bar{\sigma}_{\phi\phi}$ occurs at $\alpha a = 0.7$ and is about 30% higher than the static values.

Figures 7 and 8 also show that Poisson's ratio of the medium influences the results. It can be seen that the maximum value of $\bar{\sigma}_{\phi\phi}$ increases with the increase in Poisson's ratio of the medium. Maximum value of $\bar{\sigma}_{tt}$, however, does not seem to be affected, except for $\nu = 0.45$.

Figure 9 presents the behavior of $\bar{\sigma}_{\phi\phi}$ and $\bar{\sigma}_{tt}$ at $\theta = \pi/2$ as a function of the aspect ratio b/a for values of $\alpha a = 0.2$, 0.5, 1.0, 1.5 and 2.0. It is noted that the magnitude of $\bar{\sigma}_{tt}$ is generally higher than the magnitude of $\bar{\sigma}_{\phi\phi}$. As the aspect ratio b/a increases, both $\bar{\sigma}_{\phi\phi}$ and $\bar{\sigma}_{tt}$ decrease. This could be attributed

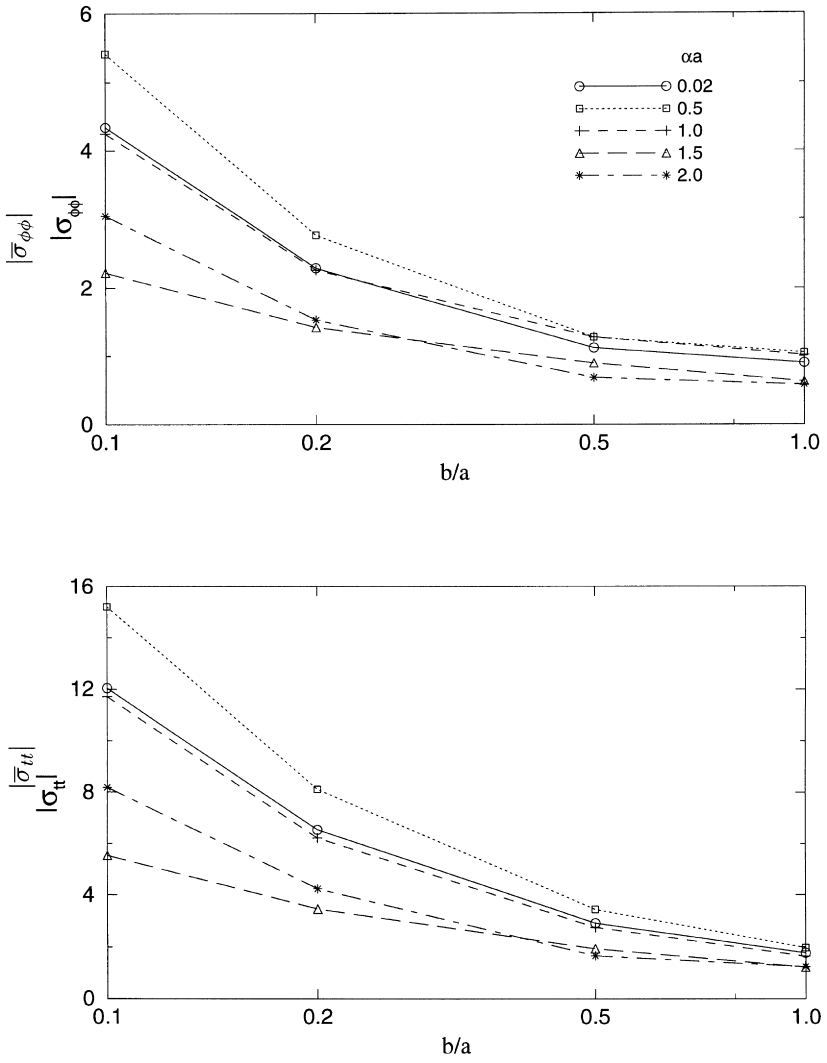

Fig. 9. Effect of aspect ratio b/a on the stresses at $\theta = \pi/2$ for $\nu = 0.35$.

to the surface at $\theta = \pi/2$ becoming increasingly planar with increasing b/a and the incident wave impinging on this surface at near grazing angle.

Tables 1 and 2 provide the maximum values of $\bar{\sigma}_{tt}$ and $\bar{\sigma}_{\phi\phi}$ in the wave number range 0.02–3.0 for values of $b/a = 0.1$, 0.2, 0.5 and 1.0. In these tables the maximum static values and their locations are given in the third and fourth columns, respectively. The next column in the tables gives the maximum values of the dynamic stresses. The frequency and location at which these maxima occur are given in the sixth and seventh columns, respectively. Finally, the percentage increase of the maximum dynamic stress concentration factor over the static value is given in the last column.

In general, the dynamic stresses are considerably higher than the static stresses. Both static and

Table 1
Maximum values of $\bar{\sigma}_{tt}$

		Static		Dynamic			
b/a	ν	$\bar{\sigma}_{tt}$ (max)	θ	$\bar{\sigma}_{tt}$ (max)	αa	θ	Percent increase
0.1	0.25	12.05	90	16.62	0.82	90	38
	0.30	12.04	90	16.75	0.78	90	39
	0.35	12.03	90	17.06	0.71	90	42
	0.40	12.03	90	17.72	0.63	90	47
	0.45	12.12	90	19.36	0.49	90	60
0.2	0.25	6.621	90	8.641	0.78	90	31
	0.30	6.587	90	8.675	0.74	90	32
	0.35	6.543	90	8.777	0.69	90	34
	0.40	6.491	90	9.033	0.61	90	39
	0.45	6.452	90	9.720	0.48	90	51
0.5	0.25	3.012	90	3.535	0.68	90	17
	0.30	2.970	90	3.518	0.65	90	18
	0.35	2.915	90	3.519	0.62	90	21
	0.40	2.842	90	3.576	0.58	90	26
	0.45	2.748	90	3.875	0.52	90	41
1.0	0.32	1.849	90	2.000	0.55	88	8
	0.30	1.813	90	1.978	0.55	88	9
	0.35	1.765	90	1.974	0.60	86	12
	0.40	1.702	90	2.084	0.65	82	22
	0.45	1.618	90	2.616	0.56	66	62

dynamic stress values are considerably large for $b/a = 0.1$; this is to be expected since at such low aspect ratio, the pore is almost like a penny-shaped crack. For the tangential stress $\bar{\sigma}_{tt}$ maximum dynamic stresses occur at $\theta = \pi/2$ in the low frequency range when αa is between 0.4 and 0.9 and are 10–60% higher than the static values, as noted earlier. Some variations in the general trend occur for $b/a = 1$ in which case the maximum dynamic stress occurs in the shadow side of the pore. The hoop stress $\bar{\sigma}_{\phi\phi}$ exhibits a somewhat different behaviour. In the case of $b/a = 0.5$ and $\nu = 0.25$, 0.30, and 0.35, for example, maximum of $\bar{\sigma}_{\phi\phi}$ occur near the pole in the shadow side of the pore at the high frequency end of the range considered. It is also noted that the absolute values of $\bar{\sigma}_{\phi\phi}$ are considerably lower than the values of $\bar{\sigma}_{tt}$; the percentage increase values for $\bar{\sigma}_{\phi\phi}$ are, however, generally higher than those for $\bar{\sigma}_{tt}$. For instance, a 107% increase can be seen for the case of $b/a = 0.5$ and $\nu = 0.25$.

5. Conclusions

We have studied the stresses in porous materials under a dynamic loading condition by using a hybrid method. We have verified the accuracy of the hybrid method by comparing our results with the analytical solution for a spherical pore. For a spheroidal pore, we have illustrated that the dynamic stress concentration factors for the tangential stress σ_{tt} and hoop stress $\sigma_{\phi\phi}$ are significantly influenced

Table 2
Maximum values of $\bar{\sigma}_{\phi\phi}$

		Static		Dynamic			
b/a	ν	$\bar{\sigma}_{\phi\phi}$ (max)	θ	$\bar{\sigma}_{\phi\phi}$ (max)	αa	θ	Percent increase
0.1	0.25	2.925	90	3.915	0.82	90	34
	0.30	3.625	90	4.933	0.77	90	34
	0.35	4.341	90	6.048	0.71	90	39
	0.40	5.092	90	7.386	0.63	90	45
	0.45	5.968	90	9.398	0.49	90	57
0.2	0.25	1.492	90	1.848	0.78	90	24
	0.30	1.886	90	2.390	0.75	90	27
	0.35	2.285	90	2.976	0.70	90	30
	0.40	2.693	90	3.659	0.62	90	36
	0.45	3.144	90	4.639	0.49	90	48
0.5	0.25	0.689	90	1.428	3.00	2	107
	0.30	0.904	90	1.549	3.00	2	71
	0.35	1.122	90	1.651	2.92	2	47
	0.40	1.315	90	1.736	0.71	90	29
	0.45	1.557	90	2.360	0.59	90	52
1.0	0.25	0.544	90	0.997	2.75	0	83
	0.30	0.721	90	1.113	2.55	0	54
	0.35	0.907	90	1.281	2.27	0	41
	0.40	1.100	90	1.586	0.74	66	44
	0.45	1.300	90	2.457	0.60	24	89

by the frequency of excitation (or wave number), geometry of the pore and Poisson's ratio of the medium. In general, the dynamic stress concentration factors are considerably higher than the quasi-static values, and in certain cases the percentage increase may reach as high as 10% over the quasi-static value.

Appendix

Assuming $\{q_B^s\}_{\text{sph}}$ is known, eqn (14) may be solved for $\{a\}$ by minimizing the least square error of the error function $\{\varepsilon\}$ defined by

$$\{\varepsilon\} = [G]\{a\} - \{q_B^s\}_{\text{sph}}. \tag{A1}$$

The square of the error ε^2, which is a scalar, is given by

$$\varepsilon^2 = \{\varepsilon^*\}^{\text{T}}\{\varepsilon\}. \tag{A2}$$

Substitution of eqn (A1) into eqn (A2) leads to

$$\varepsilon^2 = \{a^*\}^{\text{T}}[G^*]^{\text{T}}[G]\{a\} - \{q_B^{s^*}\}^{\text{T}}_{\text{sph}}[G]\{a\} - \{a^*\}^{\text{T}}[G^*]^{\text{T}}\{q_B^s\}_{\text{sph}} + \{q_B^{s^*}\}^{\text{T}}_{\text{sph}}\{q_B^s\}_{\text{sph}}. \tag{A3}$$

Minimizing the square of the error with respect to $\{a\}$ yields

$$[G^*]^{\mathrm{T}}[G]\{a\} = [G^*]^{\mathrm{T}}\{q_B^s\}_{\mathrm{sph}}. \tag{A4}$$

Since $[G^*]^{\mathrm{T}}[G]$ is a square matrix, eqn (A4) can be solved for $\{a\}$ as

$$\{a\} = [H]\{q_B^s\}_{\mathrm{sph}} \tag{A5}$$

where

$$[H] = \left([G^*]^{\mathrm{T}}[G]\right)^{-1}[G^*]^{\mathrm{T}}. \tag{A6}$$

For $p \leq N_B$, $[H]$ is the generalized inverse of $[G]$ and the uniqueness of the operation is assured (Lancaster, 1969).

References

Avanessian, V., Muki, R., Dong, S.B., 1986. Forced oscillations of an axisymmetric structure in contact with an elastic half space by a version of global local finite elements. J. of Sound and Vibration 104, 449–463.

Avanessian, V., Dong, S.B., Muki, R., 1989. Interaction of an axisymmetric body with obliquely incident seismic waves by global local finite elements. Earthquake Engineering and Structural Dynamics 18, 185–197.

Boccaccini, A.R., Ondracek, G., Mombello, E., 1995. Determination of stress concentration factors in porous materials. J. Mater. Sci. Lett 14, 534–536.

Bogan, S.D., Hinders, M.K., 1993. Dynamic stress concentrations in fiber-reinforced composites with interface layers. J. Comp. Mat 27, 1272–1311.

Danninger, H., Jangg, G., Weiss, B., Stickler, R., 1993. Microstructure and mechanical properties of sintered iron. Part 1: Basic considerations and review of literature. Powder Metallurgy International 25, 111–117.

Datta, S.K., 1997. Diffraction of plane elastic waves by ellipsoidal inclusions. J. Acoust. Soc. Amer 61, 1432–1537.

Datta, S.K., Shah, A.H., 1982. Scattering of SH-waves by embedded cavities. Wave Motion 4, 265–283.

Dong, S.B., 1981. Global-local finite element methods. In: Pilkey, W.D., Noor, A.K. (Eds.), State-of-the-Art Survey of Finite Element Methods. (Chap. 14) ASME Publication.

Goetschel, D.B., Dong, S.B., Muki, R., 1982. A global local finite element analysis of axisymmetric scattering of elastic waves. ASME Journal of Applied Mechanics 49, 816–820.

Hasselman, D.P.H., Fulrath, R.M., 1964. Effect of small fraction of spherical porosity on elastic moduli of glass. J. Amer. Ceram. Soc 47, 52–53.

Kirsch, G., 1898. Die Theorie der Elastizität und die Bedurfnisse der Festigkeitslehre. Zeitschrift des Vereines Deutscher Ingenieure 42, 797.

Maitra, A.K., Phani, K.K., 1994. Ultrasonic evaluation of elastic parameters of sintered compacts. J. Mater. Sci 29, 4415–4419.

Meguid, S.A., Wang, X.D., 1997. Wave scattering from partially-debonded inhomogeneities in advanced ceramics. Presented at the 1997 Joint ASME, ASCE and SES Summer Metting, 29 June–2 July, Northwestern University.

Morse, P.M., Feshbach, H., 1953. Methods of Theoretical Physics. McGraw-Hill, New York.

Neuber, H., Hahn, H.G., 1966. Stress concentration in scientific research and engineering. App. Mech. Rev 19, 187–199.

Olsson, P., Datta, S.K., Bostrom, A., 1990. Elastodynamic scattering from inclusions surrounded by thin interface layers. J. Appl. Mech 57, 672–676.

Panakkal, J.P., Willems, H., Arnold, W., 1990. Nondestructive evaluation of elastic parameters of sintered iron powder compacts. J. Mater. Sci 25, 1397–1402.

Pao, Y.H., Mow, C.C., 1973. Diffraction of Elastic Waves and Dynamic Stress Concentrations. Crane and Russak, New York.

Paskaramoorthy, R., Datta, S.K., Shah, A.H., 1988. Effect of interface layers on scattering of elastic waves. J. Appl. Mech 55, 871–878.

Paskaramoorthy, R., Shah, A.H., Datta, S.K., 1989. Scattering of flexural waves by a crack in a plate. Engineering Fracture Mechanics 33, 589–598.

Rossi, R.C., 1968. Prediction of the elastic moduli of composites. J. Amer. Ceram. Soc 51, 533–539.

Sternberg, E., 1958. Three-dimensional stress concentrations in the theory of elasticity. App. Mech. Rev 11, 1–4.

Wang, J.C., 1984. Young's modulus of porous materials. J. Mater. Sci 19, 801–814.

Willis, J.R., 1980. A polarization approach to the scattering of elastic waves—I. Scattering by a single inclusion. J. Mech. and Phys. of Solids 28, 287–305.